THE JOURNAL OF PHYSICAL CHEMISTRY C
A JOURNAL OF THE AMERICAN CHEMICAL SOCIETY

pubs.acs.org/JPCC

Article

Dramatic Maturing Effects on All Inorganic $CsPbBr_3$ Perovskite Solar Cells under Different Storage Conditions

Daniel Commandeur, Thomas Draper, Zainab T. Y. Alabdulla, Rong Qian, and Qiao Chen*

Cite This: https://doi.org/10.1021/acs.jpcc.1c05714

Read Online

ACCESS | Metrics & More | Article Recommendations | Supporting Information

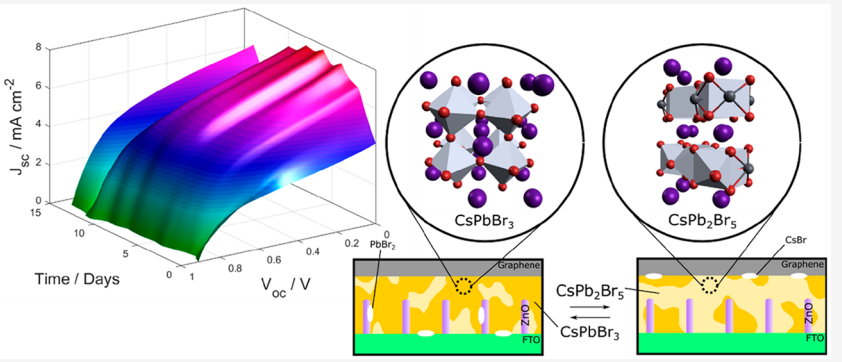

ABSTRACT: As perovskite solar cells have yielded impressive efficiency at a low cost, the focus has shifted to increase their service life as they are plagued by rapid degradation. Refreshingly, $CsPbBr_3$ solar cells built on a conductive ZnO nanowire electron transport layer with a graphite counter electrode not only avoided degradation but also showed some of the reverse trends under specific conditions, showing significant maturation over time. In this work, this phenomenon is first confirmed to be reproducible from a large sample size with on average a 40 ± 10% increase in efficiency after 2 weeks of storage. To explore the mechanisms of this positive maturing effect, samples were stored under different controlled conditions and tested regularly by using scanning electron microscopy, powder X-ray diffraction, current−voltage (*IV*) curves, and impedance spectroscopy. The samples stored in a methanol atmosphere presented a dramatic positive effect, giving a 4-fold increase in efficiency after 2 days of storage. However, in the saturated H_2O environment, the device performance rapidly degraded. By observing the solar cell performance affected by various storage conditions, including various solvent vapors, light illumination, and an inert gas (N_2), we suggest three possible complementary factors. First, solvents shifted the equilibrium of crystal phase ratio of $CsPbBr_3$ to $CsPb_2Br_5$. Second, the $CsPbBr_3$ grain size was reduced with improved electrical contact with the conductive ZnO nanowires. Finally, ion migration and accumulation lead to the formation of local p−n junctions at crystal grain boundaries with improved charge separation. This was evidenced by the increased kinetic relaxation times on ionic time scales. Rather than degrading, under appropriate conditions, these cells were able to increase in value/efficiency over storage time. By elucidating the underlying mechanisms for the $CsPbBr_3$ solar cell stability, the work offers guidelines for improving perovskite solar cell long-term efficiency.

1. INTRODUCTION

Because of their meteoric rise in efficiency and solution-based production, inorganic−organic hybrid perovskite solar cells (PSCs) have been the subject of intense research.[1−4] The major limitation to these devices is their performance stability, often requiring delicate encapsulation to retain long-term performance.[5,6] Recently, great stability increases have been achieved by exchanging the methylammonium cation with cesium, leading to the rapid development of all-inorganic perovskite solar cells, achieving efficiencies as high as 13.4%.[7,8] Without encapsulation, $CsPbBr_3$ solar cells are among the most stable devices, with excellent performance stability under high humidity (90−95% RH) and high temperature (100 °C).[9] In general, these cells could retain ∼90% of their performance after 10−130 days.[10−12] Despite such long-term stability, few works have demonstrated reversing the trend in declining performance.

A key factor for the degradation of perovskite solar cells is the generation of superoxide within the cell, which reacts with the methylammonium in the perovskite to form its constituent reactants, evidenced by Aristidou et al.[13] This process requires oxygen, moisture, and light, where the hydrophilic methylammonium cation causes the rapid infiltration of H_2O, thereby

Received: June 28, 2021
Revised: August 20, 2021

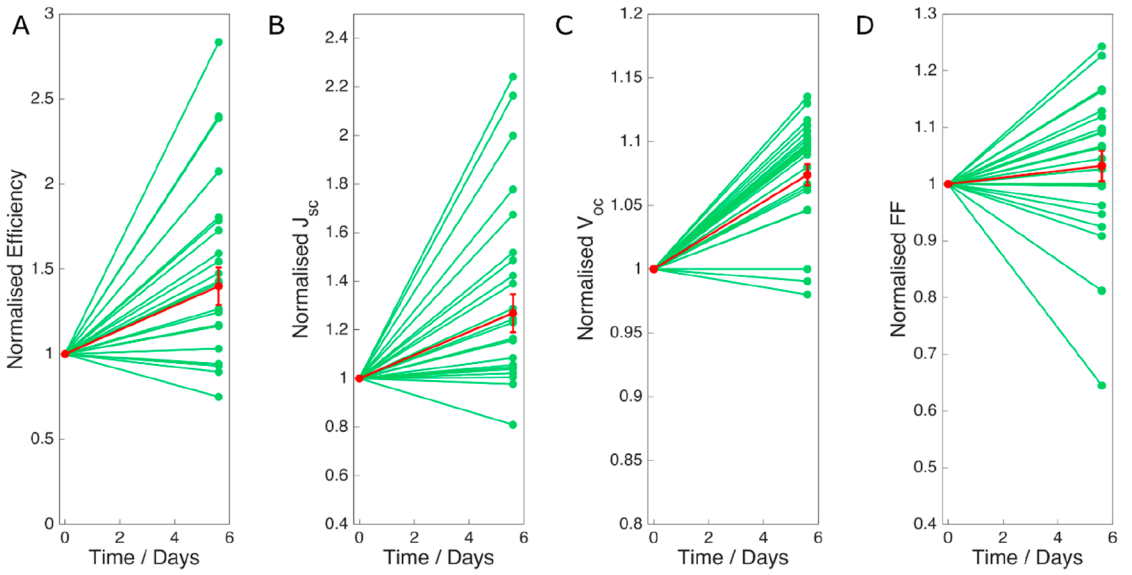

Figure 1. Solar cell parameters of a 24-cell sample size and their changes over 14 days. Each sample has an equal contribution. (A) η, (B) J_{sc}, (C) V_{oc}, and (D) FF of the cells. The red line represents the average value of each parameter.

damaging the cells. Cesium, on the other hand, is nonvolatile and chemically stable in reacting with superoxide radicals, leading to added stability.[10] To date, the degradation mechanism involved in $CsPbBr_3$, although occurring at a much slower rate, is largely unexplored, except for the accelerated degradation by high humidity.

Modest gains in solar cell efficiency over time have been previously reported, attributed to various effects. Oxygen vacancy generation in the TiO_2 electron transport layer was one of the mechanisms responsible for an efficiency doubling by light soaking over 15 min, found by Liu et al.[14] This led to a reduction in the series resistance, leading to greater device performance, though it declined over a period of days. Ginting et al. observed a permanent ~24% rise in efficiency after 24 h of storage in the dark conditions in air, which they attributed to the oxidation of spiro-OMeTAD, leading to improved hole transport.[15] By thermally aging $CsPbBr_3$ at 45 °C for 300 h, Luchkin et al. saw an increase of 35% in PCE due to the formation of p−n junctions at the grain boundaries. These junctions were formed due to ion migration. The p−n junctions promote effective electron−hole separation and, consequentially, reduced their recombination.[16] Finally a 30% increase in efficiency was observed after 1000 h of storage under N_2, for $CH_3NH_3PbI_3$ solar cells, which was attributed to the infiltration of the perovskite into the ZnO nanorods (NRs) crystal electron transport material (ETM).[17] Clearly, many different effects are at work that can lead to solar cell maturation under various storage conditions.

In this work, dramatic long-term maturing effects are measured after the storing of CsPbBr for 14 days, leading to a PCE increase of 40 ± 10%. As the solar cells were constructed by using ZnO NRs as the ETM with graphite as the hole transporting material (HTM), the aging mechanism is expected to be different from those with spiro-OMeTAD as the HTM. To determine the mechanism behind this phenomenon, a wide range of storage conditions were evaluated. The improved solar cell performance, characterized by several techniques, was confirmed in association with the increased infiltration of perovskite into the ZnO during the storage, establishing a crystallographic mechanism. The effects of ion migration and crystal phase ratio of the triclinic ($CsPb_2Br_5$) to the orthorhombic phase ($CsPbBr_3$) were also responsible for the improved performance. Finally, we demonstrated the control over maturation and understanding of degradation in these devices by exposing the samples to saturated moisture and solvent atmospheres along with light or dark conditions in N_2 or air environments. This leads to either a 4-fold increase in performance in MeOH storage or device failure in H_2O after 48 h.

2. EXPERIMENTAL METHOD

2.1. Solar Cell Construction. Full details of device construction can be found in our previous work.[18] Briefly, etched and cleaned FTO-glass substrates were spin-coated with 0.1 M zinc acetate solution, followed by annealing to convert the layer to zinc oxide seeds. Substrates were then placed face down in a growth solution overnight of 20 mM zinc nitrate and 20 mM hexamethylenetetramine for chemical bath deposition of ZnO NRs ETM. These were then subjected to light acid treatment and passivated with dip-coated TiO_2 as optimized in previous work.[18] Following this, $CsPbBr_3$ perovskite was deposited by a two-step method: a spin-coated deposition of $PbBr_2$ in dimethylformamide and then reaction with CsBr in methanol for 40 min at 50 °C. The solar cells were completed by drop-casting in a controlled area with multilayer graphite suspended in chlorobenzene as the back-contact and hole transport layer (HTM), followed by annealing at 250 °C for 5 min.

2.2. Storage in a Controlled Environment. For the benchmark study, the completed cells were kept in ambient conditions in the dark, tested on the day of completion and then 14 days later. For the controlled study under various storage conditions, samples were individually stored, covered by aluminum foil to block out light in the dark samples, or stored under illumination for contrasting measurements. The containers were filled with N_2 gas for the dry samples before sealing. The phials containing the samples to be exposed to solvent were placed in larger sealed jars, containing 20 mL of

https://doi.org/10.1021/acs.jpcc.1c05714
J. Phys. Chem. C XXXX, XXX, XXX−XXX

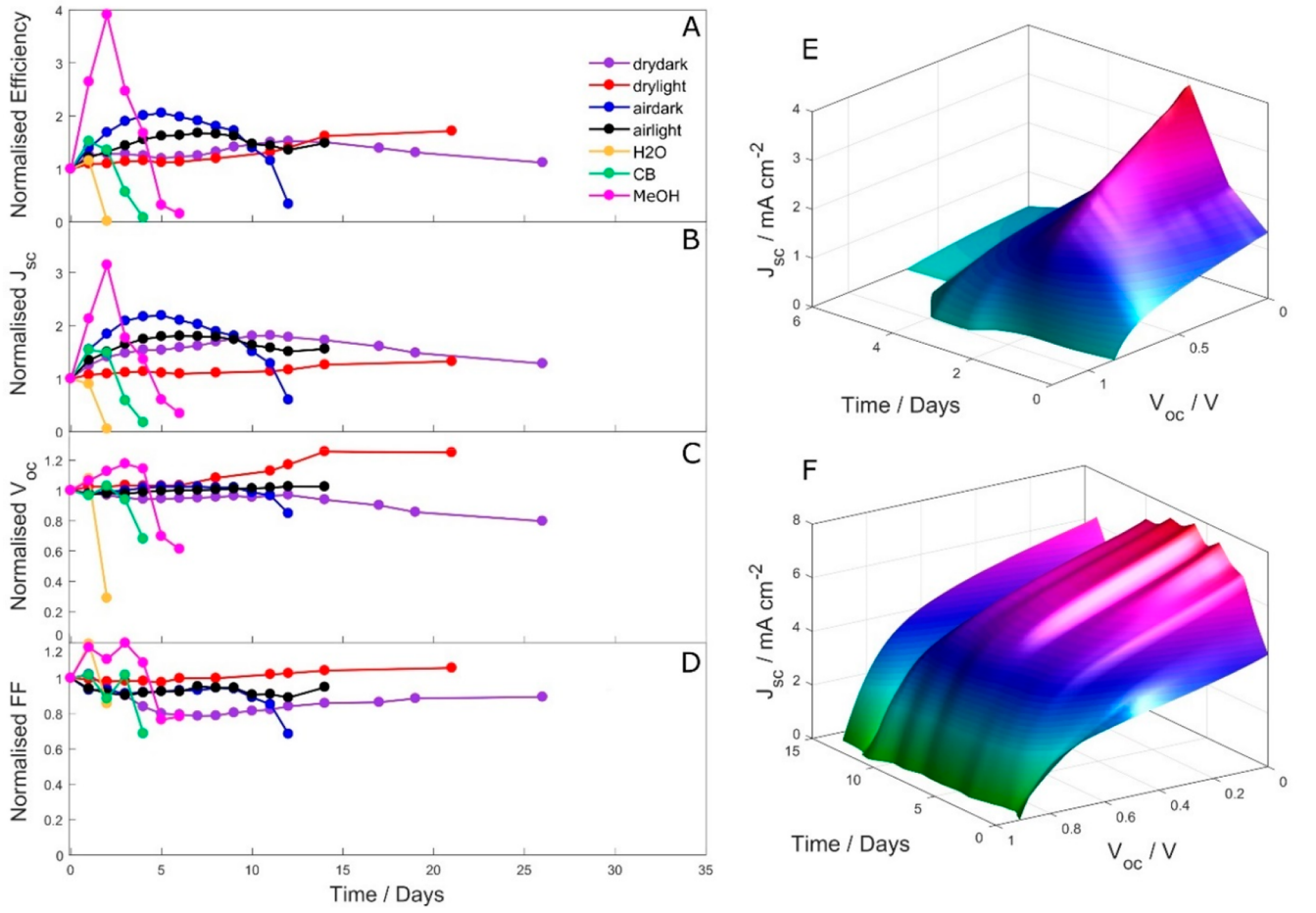

Figure 2. Normalized average parameters of solar cells stored in various conditions with (A) solar cell η, (B) J_{sc}, (C) V_{oc}, and finally (D) FF. The surface plots of *IV* curves of the cells through time are shown in (D) stored in MeOH and (F) stored under illumination in air.

designated solvent (see Figure S1). Methanol and chlorobenzene were targeted due to their presence in the device construction. The samples were characterized daily.

2.3. Sample Characterization. Samples were removed from their storage conditions to be characterized by top-down scanning electron microscopy (SEM, JSM 820M, Jeol) and powder X-ray diffraction (XRD, Siemens D500) to track the morphological and crystallographic evolution, respectively. To analyze the device performance alongside optoelectronic charge transfer effects, cells were measured by cyclic voltammetry to obtain current−voltage (*IV*) behavior followed by electrochemical impedance spectroscopy (EIS) under illuminated conditions by using a calibrated solar simulator (Oriel LCS-100, Newport) with a built-in AM 1.5G filter, calibrated to 100 mW/cm^2. The *IV* curves were recorded with a cyclic scan of 20 mV/s to determine the hysteresis. The EIS was performed with a 10 mV sinusoidal modulation, with frequency varied from 50000 to 0.1 Hz, in addition to a DC voltage. Both these measurements were performed by using a PalmSens 3 electrochemical controller with PS trace 4.5 (PalmSense BV) and Elchemea analytical software to process the equivalent circuit fit. To ensure XRD diffractograms were taken from the same location on the sample each time, samples were secured to the sample stage with the same orientation at the same marked point. Images taken by SEM of the sample surface were of regions identified by low magnification to be representative of the entire film surface.

3. RESULTS AND DISCUSSION

3.1. Reproducible Maturing Effects. As the dramatic efficiency improvement in perovskite solar cells over time has rarely been reported previously, it is vital to demonstrate the reliability and the reproducibility of the observation before we can investigate the underlining mechanism. Therefore, to confirm this phenomenon, a large sample size of 24 solar cells was studied by measuring their performance on the first day of construction (day 0) and then again after 14 days of storage in dark ambient conditions. The results of this initial study are displayed in Figure 1, measuring the four core parameters of the solar cell efficiency η, short-circuit current J_{sc}, open-circuit voltage V_{oc}, and fill factor (FF). This study confirms the regular occurrence of performance improvement during storage. There were 19 out of 24 samples that displayed an increase in the power conversion efficiency (Figure 1A). Some of the cells' degradation is associated with the possible inhomogeneity of the active layer. Nevertheless, it can be summarized by the 40 ± 10% average growth in efficiency. The average initial efficiency of 1.81 ± 0.16% was increased to the average final efficiency of 2.53 ± 0.19% after 14 days for the 24 solar cells. The red lines in Figure 1 represent the change of the averaged values of the parameters. The power conversion efficiency depends on the product of J_{sc}, V_{oc}, and FF. The aging effects on these parameters are shown in Figures 1B−D.

https://doi.org/10.1021/acs.jpcc.1c05714
J. Phys. Chem. C XXXX, XXX, XXX−XXX

Although increases could be observed in all three parameters, the average increase in FF was within the error, implying that the recombination in the bulk perovskite phase and the parasitic resistances of the cells did not greatly change over time. Conversely, distinctive gains were seen in both J_{sc} and V_{oc} values which are responsible for the efficiency maturing effect. First, a modest rise in the V_{oc} of 8 ± 1% was observed. V_{oc} is dominated by the difference in quasi-Fermi levels between the intrinsic layer and the HTM, defined by the material band structures. Enhancements in V_{oc} often indicate the reduced number of pinholes and defects in the perovskite film, which in turn reduce the number of deep states within the bandgap that occur at the edges of grain boundaries.[19] Most importantly, a significant increase in the J_{sc} was observed after 14 days of storage in the dark. The averaged J_{sc} showed an increase of 25.0 ± 8%, with the averaged J_{sc} increased from 5.2 to 6.5 mA cm^{-2} after 14 days in storage. From the 24 cells, the highest J_{sc} of 10.3 mA cm^{-2} was observed from one of the cells stored in the dark for 14 days, yielding the greatest enhancement in the performance. The J_{sc} is typically governed by light absorption and quantum efficiency, the latter of which relies on efficient extraction of photogenerated charge at the ETM and HTM interfaces.[20] In the only other report of increased efficiency after long storage time for solar cells built on ZnO NWs, Wu et al. attributed this effect on the sinking of $MAPbI_3$ between the NW array over time with increased surface contact for charge extraction.[17] A similar mechanism could be responsible in this study for the increased J_{sc}.

The degree of hysteresis (DoH) was also calculated via eq S1, quantifying the difference in *IV* plots depending on the direction of the linear potential sweep. Despite being a vital factor in the degradation of $MAPbI_3$,[13] the values of DoH remained much smaller in $CsPbBr_3$ solar cells, shown in Figure S2A. It increased by 7% from the initial value of 0.041 ± 0.008. However, the small increase in the DoH value might be significant in explaining the maturing effects of storage.

3.2. Storage Conditions and Solar Cell Parameters.

To identify the causes of the maturing cells stored in ambient conditions in the dark, different devices were stored in seven controlled conditions that might affect the cell performance. The conditions can be catalogued as the solvent effects and light/gas effects. To study solvent effects, cells were placed in saturated environments of methanol (MeOH), chlorobenzene (CB), and water (H_2O). These solvents were chosen as they feature commonly in the device production in the case of MeOH and CB, which could be trapped within the perovskite solar cell to facilitate the maturing effects in dark conditions. H_2O was selected as atmospheric moisture often attributes to the degradation of PSCs.[13] To track the impact of exposure to light during PCE tests, along with effects of atmospheric O_2, the final four samples were kept in the following configurations: room light in air (air light); room light in N_2 gas (dry light); dark in air and dark in N_2 gas (air dark and dry dark). The tracking of the normalized η, J_{sc}, V_{oc}, and FF can be found in Figures 2A–D, while DoH can be found in Figure S2B. The cells were tested daily for up to 26 days, and the measurements were averaged over the three different cells. The raw *IV* curves from selected cells for each storage condition can be found in Figures S3 and S4.

Surprisingly, all samples begin with an increase in η after the first day of storage in various conditions—the most dramatic of which belongs to the sample stored in MeOH, which rose to nearly 4 times its original efficiency after 2 days of storage, for which the single-cell *IV* curves as a function of storage days are shown in Figure 2E. This is accompanied by significant increases in the associated solar cell parameters: a 3-fold increase in J_{sc} and ∼20% gains in V_{oc} and FF. However, this is followed by an equally steep drop off in performance, implying that any interaction with MeOH in the solar cell could have irreversible effects on the interface structures which have a strongly negative effect on the core parameters. The sample stored in CB, on the other hand, displayed a similar pattern of efficiency change, though far more modest, where only J_{sc} increased by 50%, while V_{oc} and FF remained steady until significant degradation in performance after 4 days in storage in CB. The difference in the solvent effects between MeOH and CB relies on the solubility difference of CsBr, determined by the polarities of MeOH (0.762) and CB (0.188). Hence, it is expected that MeOH with higher CsBr solubility has a more significant maturing effect, enhancing the performance dramatically at the beginning followed by rapid deterioration. Although a slight initial increase in performance was observed due to a temporary boost in FF, the storage in a saturated H_2O environment rapidly degraded device performance with reduced efficiency on day 2. It can be seen in Figure S2B that both H_2O and CB caused large increases in the hysteresis of the cells, a common feature in PSCs experiencing degradation.[21] Moisture can decompose the perovskite containing lead due to the formation of $Pb(OH)_2$.

The other four samples (dry dark, dry light, air dark, and air light) showed far greater resistance to their respective storage conditions. The samples stored under N_2 (dry dark and dry light) had no decline in cell efficiency, even up to 26 days after construction. Both these samples had a slow rise in efficiency, likely due to the small amount of trapped solvent, which gradually evaporated from the device. Under a dark condition in N_2, the J_{sc} increased slowly while the FF and V_{oc} decreased. The removing of the trapped solvent from the perovskite layer limits both the positive or negative maturing effects. The dry light sample comparatively held stable values for J_{sc} and FF with an eventual significant increase in V_{oc}, potentially due to the improvement of perovskite crystal quality with fewer trap states from defects. This would explain the gains in efficiency for the illuminated samples showing greater longevity, finishing higher than their corresponding dark samples. With the light illumination cycles, the mobile charge was generated, separated, and neutralized. The created internal electrical potential will drive the slow movement of ions which could help to reduce crystal defects. A similar principle can be applied to thermal annealing. However, the photoannealing operated at room temperature and has much better control than the thermal process.

Tracking the parameters of the dark air sample day by day yields important information about the interim period performance of the samples presented in Figure 1. Strong increases in J_{sc} are seen followed by a reduction on day 12, along with a collapse in V_{oc} and FF. The maturing process in this daily measurement is accelerated with respect to the continuous storage in the dark for 14 days. This acceleration is likely due to the daily measurements of the powder XRD, SEM, and illuminated *IV* measurements and EIS measurements.

Figure 2F shows the rise and fall in efficiency for a single cell from the air light sample. The positive effects are likely the sum

https://doi.org/10.1021/acs.jpcc.1c05714
J. Phys. Chem. C XXXX, XXX, XXX−XXX

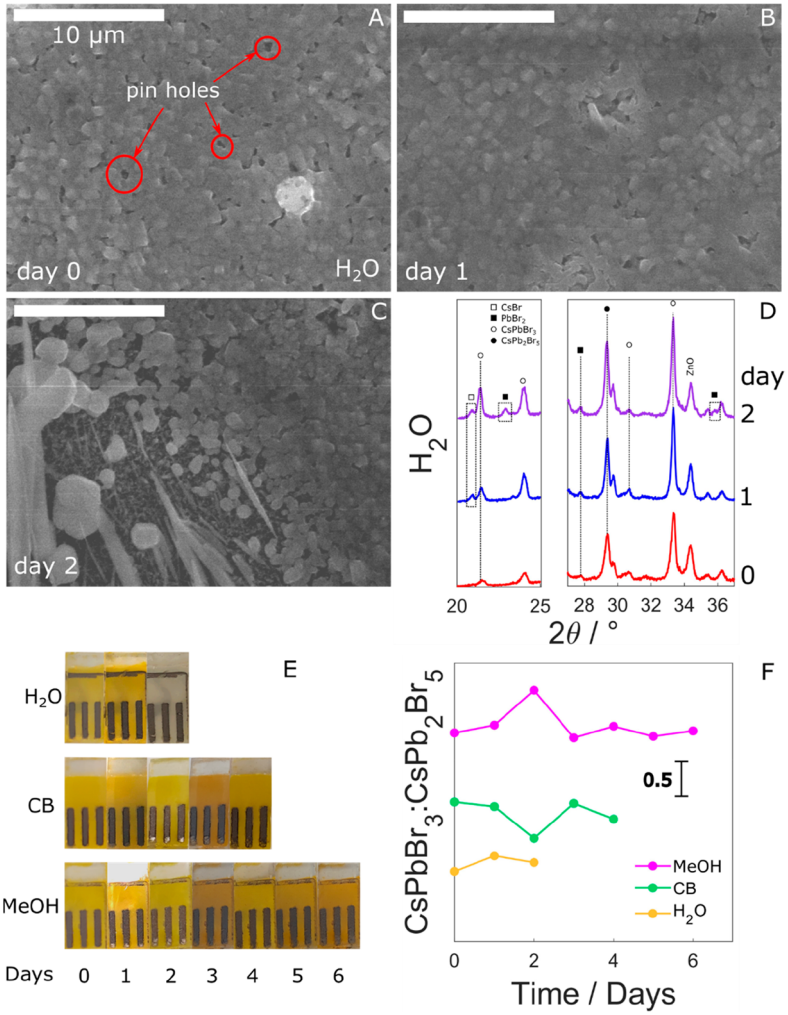

Figure 3. (A–C) Top-down SEM images from day 0 to day 2 for the sample stored under saturated H_2O conditions. (D) Powder XRD plots of the perovskite in stored solar cells. (E) Photographs were taken daily of the samples. (F) Ratio of phases based on the ratio of peak intensities.

of constituent conditions, which were identified via SEM and powder XRD characterization later.

3.3. Moisture and Solvent Effects. The storage condition with the most negative effect on device performance was the high humidity chamber (H_2O), the progress of which can be seen in Figure 3. On the day of construction, some CsBr crystals (white dots) were visible on the surface along with many pinholes (Figure 3A). Remarkably, many surface defects were healed by day 1 (Figure 3B). With continuous exposure to moisture, the degradation of $CsPbBr_3$ film was observed on day 2 forming rod structures and agglomerates (Figure 3C). At this stage, the sample color changed from yellow to white, permanently, shown in Figure 3E. The powder XRD in Figure 3D shows an initial growth in orthorhombic $CsPbBr_3$ perovskite peaks (ICDD #30-0697) at 33.5° and 22.0°, followed by the rise of new peaks at 21.5°, 22.7°, 27.9°, and 35.8° after 2 days exposure with water vapor. These peaks are assigned to CsBr and $PbBr_2$, suggesting the decomposition of $CsPbBr_3$. Additional peaks confirm the presence of $CsPb_2Br_5$ tetragonal phase (ICDD#25-0211), common in the $PbBr_2$-rich, two-step reaction devices. Full XRD data can be found in Figures S5 and S6. These results indicate that, initially, H_2O promotes the growth of $CsPbBr_3$, which is a known effect of moisture in the precursor solution.[23] The improved crystal quality with a reduced pinhole layer leads to the improved efficiency and FF observed on day 1. Once saturated on day 2, however, the perovskite breaks down into its constituent components, CsBr and $PbBr_2$.

The devices stored in MeOH and CB reached an equilibrium between orthorhombic $CsPbBr_3$ and triclinic $CsPb_2Br_5$ crystal phase, respectively, via the following reactions:

$$CsPbBr_3 + PbBr_2 \rightleftharpoons CsPb_2Br_5 \quad (1)$$

$$2CsPbBr_3 \rightleftharpoons CsPb_2Br_5 + CsBr \quad (2)$$

Both the CsBr and $PbBr_2$ were available in excess, due to the incomplete solid-state reactions, with bright particles of the former species visible for all the samples imaged on day 0 (Figure 4A). The presence of $PbBr_2$ has been confirmed by XRD but is likely to be closer to the NWs, as it was deposited in the first step of perovskite synthesis. The ratio of orthorhombic to tetragonal phases was measured by the integration of the $CsPbBr_3$ peaks across the full diffractogram divided by the integration of the $CsPb_2Br_5$ peaks. The results are displayed in Figure 3F.

The phase ratio in the MeOH sample increases initially, suggesting the increase in the $CsPbBr_3$. Meanwhile, the phase

https://doi.org/10.1021/acs.jpcc.1c05714
J. Phys. Chem. C XXXX, XXX, XXX−XXX

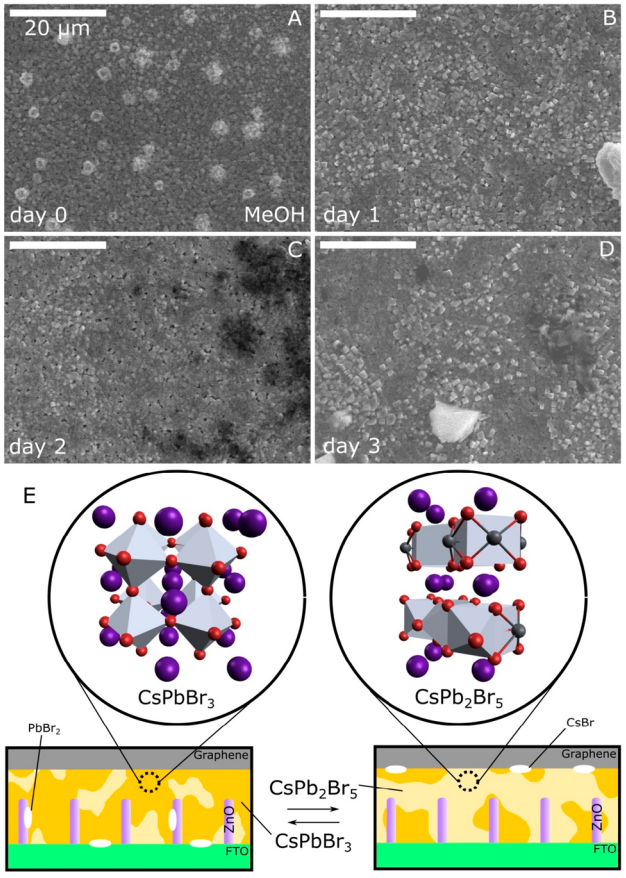

Figure 4. (A–D) Top-down SEM images from day 0 to day 3 of the samples stored in a methanol environment. (E) Models to show the effect of the crystal phase ratio shifting from $CsPbBr_3$ to $CsPb_2Br_5$.

ratio in the CB sample decreases initially, suggesting the increase in the $CsPb_2Br_5$. Despite evidence to show that a small quantity of $CsPb_2Br_5$ can be beneficial for the performance of PSCs to reduce electron–hole recombination, the abundance of this phase leads to great problems with light absorption in the device.[22] Finding sophisticated methods of producing high purity perovskite phase has led to great increases in efficiency recently.[11,23] This work, therefore, provides a possible alternative to achieve this aim using MeOH as an effective maturing solvent by improving the quality of $CsPb_2Br_5$. As we mentioned before, the effect of MeOH is determined by the solubility of CsBr. With high solubility, there are several positive effects of MeOH to improve the quality of the $CsPbBr_3$ thin film. It allows the completion of the liquid–solid reaction between CsBr (liquid) and $PbBr_2$ (solid) by improving the mass transportation of CsBr. The same mechanism could also promote the transition from $CsPb_2Br_5$ to $CsPbBr_3$, which is important for the two-step synthesis method. Meanwhile, it helps to facilitate the Ostwald ripening of the $CsPbBr_3$, allowing the dissolving of small crystals while growing the large $CsPbBr_3$ crystals. Following these processes, the number of surface defects was reduced and the overall quality of the $CsPbBr_3$ thin film was improved, which is responsible for the increase in cell efficiency associated with the increased J_{sc}.

The ripening mechanism was directly observed under SEM shown in Figure 4A–D. The top-down SEM images show a complete dissolution of surface CsBr, from day 0 to day 1, and the merging of $CsPbBr_3$ grains into day 2. Beyond this time, the solvent begins attacking the $CsPbBr_3$ phase, forming aggregates on the surface as the reaction is reversed, visible in Figures 4C,D. This was further evidence by a reversed phase shift in XRD shown in Figure 3F. The formation of a higher purity $CsPbBr_3$ explains the behavior of device performance measured in Figure 2, as this will strongly improve the values of J_{sc}, V_{oc}, and FF.[11] The shifting of phase equilibrium mechanism is depicted in Figure 4E alongside their crystal structure models. The accompanying fall in the $CsPbBr_3$:$CsPb_2Br_5$ ratio after day 2 degrades the performance. Conversely, some CsBr was still visible on the surface of the CB sample through time due to the poor solubility of CsBr in CB. The surface SEM and powder XRD patterns can be found in Figure S7.

3.4. Light and Air Effects. The progression of solar cell parameters through time for dry dark, dry light, air dark, and air light storage conditions was more gradual, although characterization revealed key information about the maturation effect. The samples stored under N_2 conditions showed remarkable evolution in morphology over the study time, shown in Figure 5. Significant merging of grains is seen in both light and dark samples. In the dry dark sample (Figures 5A–C), the vertically aligned ZnO nanorods became gradually less visible due to the formation of large perovskite grains over the surface of the rods, giving a smoother appearance up to day 14. Comparatively, the dry light sample (Figures 5D–F) showed an initial fusing of grains on day 5, followed by their reformation and sinking between the ZnO NRs on day 14. This trend is complemented by information extracted from the powder XRD peak width of the prominent $CsPbBr_3$ peak at 33.6°. The nanocrystalline domain size is proportional to the inverse of the full width at half-maximum (FWHM) described by the Scherrer equation.[24] The results are plotted against maturing time in Figure 5G, displaying constantly increasing FWHM for the dry dark sample as well as a reversible climb and then fall for the dry light sample. Figure 5H shows little effect on the phase ratio. This mirrors the SEM observation. The nanocrystalline domain size is initially shrinking in both samples, allowing the large grains to fit between the NRs, which in turn increases surface contact and therefore reduces charge transfer resistance. This explains the dramatic increase in J_{sc} for the dry dark sample as the charge is more effectively transferred to ETM, alongside the fall in FF as smaller grains mean greater recombination in the bulk.

As far as the authors are aware, this is the first observation of grain shrinking of perovskite material, under dry inert conditions, which is responsible for the variation of solar cell performance. Ion diffusion within the $CsPbBr_3$ material has been directly observed before.[25] Under our conditions, the ion diffusion and recrystallization process were accelerated by the light illumination and voltage bias applied during the IV and EIS tests. The ion diffusion could result in the crumbling of large crystals as well as the buildup of Br^- at the local n-type doping center and the interface between the perovskite and graphite.[16] From the SEM images in Figure 5, the fragmented crystals filled the gaps between the ZnO NRs which act as separators. Such a phenomenon occurred more strongly in the dark sample than in the light sample, where the unbiased illuminated maturing process allowed the recovery of Br^- distribution equilibrium.[25,26] Also, the mixing of higher content $CsPb_2Br_5$ might encourage the recrystallization of $CsPbBr_3$ since such samples contain a higher density of defects and

https://doi.org/10.1021/acs.jpcc.1c05714
J. Phys. Chem. C XXXX, XXX, XXX–XXX

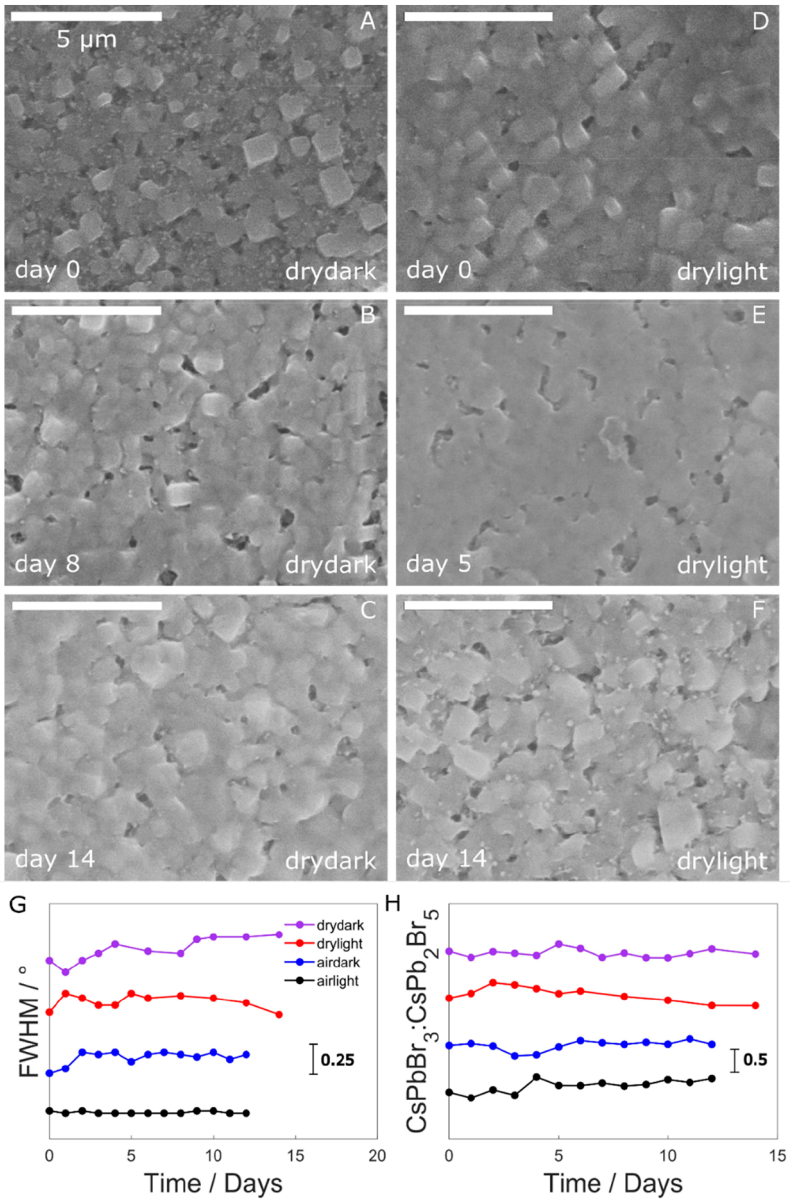

Figure 5. Top-down SEM images for dry dark conditions through time: (A) day 0, (B) day 8, and (C) day 14. SEM images for dry light conditions found in (D), (E), and (F) are for day 0, 5, and 14, respectively. (G) XRD peak FWHM for the $CsPbBr_3$ peak at 33.6°, for samples under dry, air, illuminated and dark conditions. (H) $CsPbBr_3$ to $CsPb_2Br_5$XRD peak intensity ratio over time.

domain interfaces. The possible recovery in the light sample explains why the FF and J_{sc} do not change much over the experimental time frame with only V_{oc} showing a steady rise. This observation suggests that during the fragmentation and recrystallization process the deep trap states within the $CsPbBr_3$ band gap were gradually filled up. Similar results were observed with light soaking for 24 h, leading to an increase in V_{oc}.[27] The phase ratios of the dark dry sample showed no significant swing either way, while under illumination a swing to greater $CsPbBr_3$ content occurred, followed by a reduction until reaching a plateau at day 12. Such behavior has been previously reported by Shen et al. in nanosheets of the same phases, where illumination provided sufficient energy for the phase conversion of $CsPb_2Br_5$ to $CsPbBr_3$.[28]

For the dark sample stored in air, there was minimal change in the phase ratio, although an increase in FWHM in XRD peaks was observed (Figure 5G). This confirms the grain shrinking was not hindered by the presence of O_2 or moisture. Conversely, the light air sample did not show any significant change in nanocrystalline domain size but did show a nonreversible crystal phase shift toward the orthorhombic structure. This permanent growth in $CsPbBr_3$ content confirmed that the phase transition was driven by light illumination, possibly helped by the residual solvent, such as MeOH, which is consistent with the previous study.[29]

The SEM images found in Figure 6 agree with the XRD results, showing similar progress for the samples stored in light and dark conditions in air. The only major difference is that bright spots appeared at the surface of the perovskite layer for the dark air samples on day 11. Such bright spots were also observed in the SEM images in Figure 3A, which were assigned to the CsBr crystals formed after moisture attack since they were not observed under dry conditions. It was proposed that

https://doi.org/10.1021/acs.jpcc.1c05714
J. Phys. Chem. C XXXX, XXX, XXX−XXX

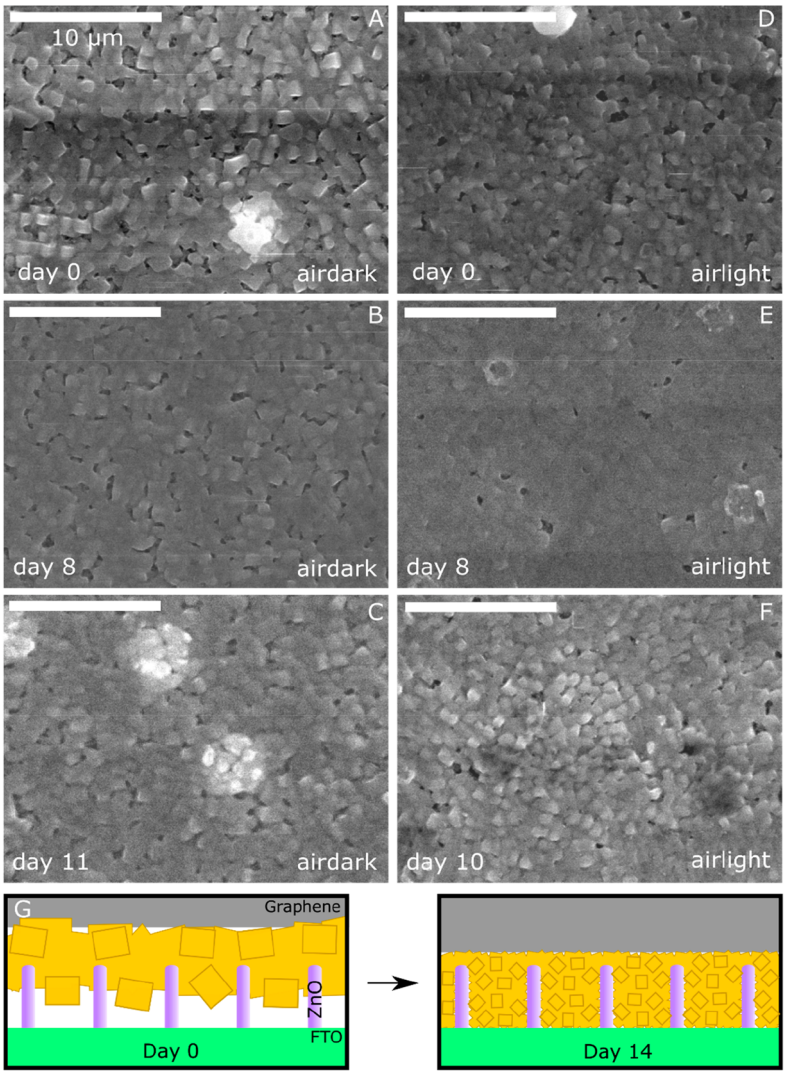

Figure 6. Top-down SEM images for samples stored in air with samples kept in the dark on (A) day 0, (B) day 8, and (C) day 14. The samples kept under constant illumination are shown in (D) day 0, (E) day 5, and (F) day 10. (G) Schematic display of grain shrinking mechanism after storage.

H_2O is responsible for the decomposition of $CsPbBr_3$ to yield the constituent $PbBr_2$ and CsBr.[30] Such permanent damage to the $CsPbBr_3$ thin film caused the rapid degradation in the cell performance with the observed reduction of FF, J_{sc}, and V_{oc}. This phenomenon was less pronounced in illuminated samples since the ion diffusion was driven by the photons, which can somehow reverse the $CsPbBr_3$ decomposition. The increased concentration of mobile ions due to the illumination is also likely to be responsible for the large rise in hysteresis, observed in Figure S2B.[15]

3.5. Storage Conditions and Impedance Parameters.

To confirm and quantify the effects of ion migration and electron−hole recombination on the solar cells during their storage, EIS was performed under illumination, under the short circuit condition. For freshly prepared samples, Nyquist plots displayed typical dual arcs (Figures 7A,B). However, after 24 h of storage, a prominent induction loop feature became visible at an intermediate frequency, with the exception of the sample stored in H_2O vapor (Figure S8). As far as the authors are aware, this is the first reported induction loop produced over time. The absence of inductive effect initially is likely due to the Br^- ions gradually moving through the sample.

The surface polarization model proposed by Ghahremanirad et al. was used to fit the data.[31] This model explains the feature as additional potential formed by the accumulation of positive charge at the anode, likely caused by ionic migration due to slow equilibration. Vitally, by using the model's lumped equivalent circuit, we determined the values of kinetic relaxation time of charge, τ_{kin}, and steady-state recombination current density, j_{rec}, using the following equations and plotted in Figures 7C,D.

$$\tau_{kin} = \frac{L}{R_L} \tag{3}$$

$$j_{rec} = \frac{\beta k_B T}{q R_{rec}} \tag{4}$$

where k_BT is the thermal energy, q is the elemental charge, β is an ideality factor equal to unity, and L, R_L, and R_{rec} are parameters measured by the surface polarization equivalent circuit (Figure 7E). Also included are two capacitors, Q_1 and

https://doi.org/10.1021/acs.jpcc.1c05714
J. Phys. Chem. C XXXX, XXX, XXX−XXX

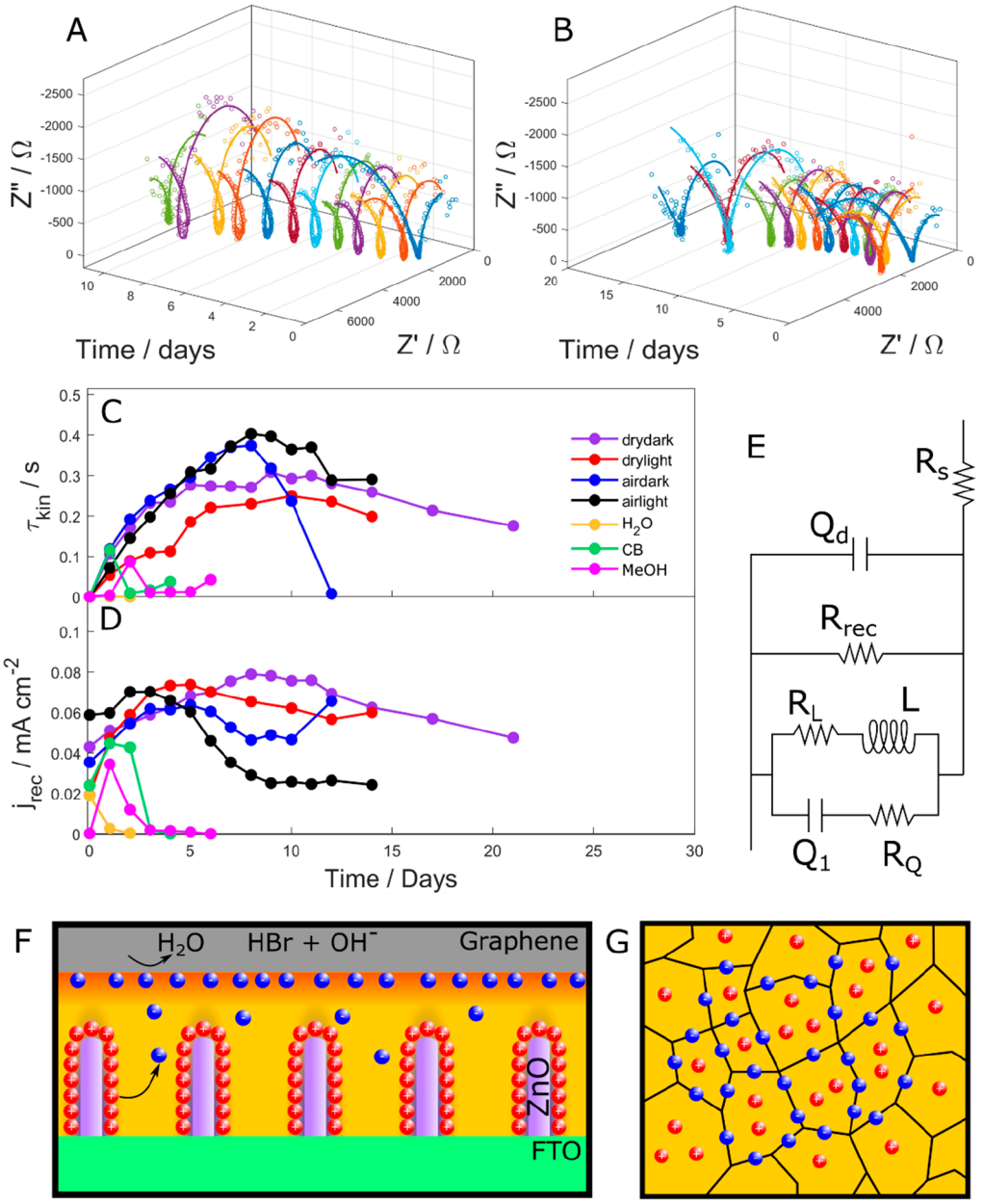

Figure 7. Evolution of the impedance spectroscopy data over time, with experimental data (circles) and surface polarization model fitting (lines) for (A) the dark air sample and (B) the light air sample. (C) and D) show the values of τ_{kin} and j_{rec} evolving through time for the cells under different storage conditions. (E) The lumped equivalent circuit model for the EIS data.[31] (F) The model describes the ion migration and accumulation, with Br^- (blue spheres) accumulating at both the cathode and grain boundaries. (G) Conversely, immobile V_{Br}^+ (red spheres) are formed at the anode interface and in the crystal grain bulk.

Q_d, corresponding to the various parallel contributions from the surface charging and the dielectric capacitance, respectively.

The model stipulates that a polarized region at the ETM/perovskite interface occurs due to a highly localized collection of halide vacancies, which was confirmed by Weber et al. using time-resolved Kelvin probe force microscopy.[32] This was observed alongside a diffuse space charge layer of halide ions distributed toward the electrostatic double layer at the HTM/perovskite interface. Greater τ_{kin} implies a slower rate of halide ions returning to the ETM interface, becoming redistributed through the light-sensitive layer. Furthermore, lower j_{rec} will be beneficial to the solar cell due to less electron−hole recombination.

Figure 7C displays the effect of storage condition on the kinetic relaxation time constant as a function of storage time under different conditions. Other than the sample exposed to high humidity, all samples showed a rise in τ_{kin} over the first few days. For the samples in solvent saturated conditions, the initial increase in τ_{kin} is likely to have a positive effect on the efficiency of the cell. However, the rapid decrease in τ_{kin} could cause a decrease in cell performance as demonstrated in Figure 2A. The negative effects of the moisture are more obvious since there was neither a measurable τ_{kin} value nor the induction feature. The solvent and moisture effects originated

https://doi.org/10.1021/acs.jpcc.1c05714
J. Phys. Chem. C XXXX, XXX, XXX−XXX

from the chemical corrosion process. After the rapid corrosion by the solvent vapor for 2 days, the ion migration is stifled, and thus no significant surface polarization can occur afterward.

The steady rise of τ_{kin} for the samples stored in air and N_2 indicates the compound accumulation of interstitial Br^- and corresponding vacancies, V_{Br}^+, near the HTM (graphite) and ETM (ZnO NRs), respectively, after the voltage sweep and light illumination during the repeated PEC and EIS measurements. The concentrations of liberated mobile ions at the interfaces increase with the sample age, resulting in a reduction in ion mobility. Hence, the samples required a longer duration for the distribution of the charges evenly, represented by a large τ_{kin} value.

The samples stored in air showed the largest τ_{kin}, which is likely due to the reaction of Br^- at the surface with the surface-adsorbed OH and H_2O to form HBr, delaying their return to the bulk perovskite.[32] For the samples stored in the dark air condition, the ions are largely immobile in storage. Therefore, HBr will quickly build up and cause the corrosion of the perovskite, as seen with the samples exposed to solvent (H_2O). As the remaining ions are more mobile, the removal of Br^- and the corrosion of the cell will lead to quick relaxation. This results in the collapse of τ_{kin} in the dark sample alongside its decline in efficiency after 7 days in storage, reaffirming the results from Figure 6. Conversely, for the light air sample, the relaxation time was further increased after 7 days in storage to reach its largest value. The photoexcitation of the perovskite increased ion and charge carrier mobilities, which helps to repair the corrosion defects in the perovskite material. This is associated with the larger hysteresis observed in this sample since the relaxation kinetics are slower. For the samples stored in dry conditions (in N_2), similar rises in τ_{kin}, were also observed. In the absence of moisture, the increased local ion concentration does not lead to the corrosion and degradation of the perovskite crystals, which is essential for stable cell performance.

The recombination current shown in Figure 7D confirms the formation of local p−n junctions along grain boundaries, associated with the surface polarization and ion migration, reducing electron−hole recombination by increasing charge separation, displayed in Figures 7F,G. This follows the reduction in j_{rec} with the increase in τ_{kin}. As expected, the recombination current increases with the reduction in crystal grain size, as recombination occurs predominantly along the grain boundaries within the perovskite layer. The time-dependent behavior of j_{rec} in Figure 7D is very similar to the j_{sc} in Figure 2B, indicating that the current j_{sc} value is limited by the defects and crystal sizes. Hence, there is great potential in optimizing the material interfaces within the cells with increased j_{sc} at reduced j_{rec}.

4. CONCLUSION

In summary, reproducible and significant maturing effects are observed in $CsPbBr_3$ solar cells based on ZnO NW electron transport layers and graphite hole collectors. The efficiency on average rises by 40 ± 10% after 2 weeks of storage under ambient dark conditions, the largest reported in the literature to date. These gains are constituted by a 25 ± 8% gain in j_{sc} alongside an 8 ± 1% increase in V_{oc}. To isolate the causes of maturation, solar cells were kept in various storage conditions representing key solvents used in the production, atmospheric moisture, and light illumination alongside control samples kept under N_2. It was found that storage in a methanol atmosphere accelerated the maturing process, yielding efficiency 4 times greater than the fresh sample. Conversely, high humidity storage prevented this effect and critically damaged performance after two days. To gain new insights into the underlying processes, the samples were observed by powder XRD, SEM, and EIS leading to three key mechanisms responsible. Changes in the dynamic crystal phase ratio between $CsPbBr_3$ and $CsPb_2Br_5$ had the strongest effect, followed by grain shrinking, allowing the perovskite to make better contact with the ZnO ETM. Finally, ionic migration of Br^- aided charge separation by forming p−n junctions at grain boundaries. This was confirmed by EIS, showing large changes in kinetic relaxation time within a window associated with the ionic transport time scale. These results not only point to a permanent increase in efficiency based on particular storage conditions, leading these solar cells closer to commercialization, but also expand the understanding of degradation resistance in inorganic perovskite solar cells, shedding light on an unexplored field.

■ ASSOCIATED CONTENT

Supporting Information

The Supporting Information is available free of charge at https://pubs.acs.org/doi/10.1021/acs.jpcc.1c05714.

The equation to calculate the degree of hysteresis (DoH), a schematic depicting the storage conditions, the DoH plotted for 14 days in various storage conditions, *IV* curves over the storage time for all the samples, powder XRD patterns against time for all samples, SEM images of the chlorobenzene sample along with finally, and the measured EIS data for all samples with equivalent circuit model fits (PDF)

■ AUTHOR INFORMATION

Corresponding Author

Qiao Chen − *Department of Chemistry, School of Life Sciences, University of Sussex, Brighton BN1 9QJ, U.K.*; orcid.org/0000-0001-5424-4818; Email: Qiao.chen@sussex.ac.uk

Authors

Daniel Commandeur − *Department of Chemistry, School of Life Sciences, University of Sussex, Brighton BN1 9QJ, U.K.*; orcid.org/0000-0002-7179-2370

Thomas Draper − *Department of Chemistry, School of Life Sciences, University of Sussex, Brighton BN1 9QJ, U.K.*; orcid.org/0000-0001-6466-8796

Zainab T. Y. Alabdulla − *Chemistry Department, College of Education of Pure Science, University of Basrah, Basra 61004, Iraq*

Rong Qian − *National Centre for Inorganic Mass Spectrometry in Shanghai, Shanghai Institute of Ceramics, Chinese Academy of Sciences, Shanghai 200050, P. R. China*; orcid.org/0000-0002-4732-5553

Complete contact information is available at: https://pubs.acs.org/10.1021/acs.jpcc.1c05714

Notes

The authors declare no competing financial interest.

■ ACKNOWLEDGMENTS

The authors thank the University of Sussex, School of Life Sciences, for the funding of this work.

REFERENCES

(1) Kojima, A.; Teshima, K.; Shirai, Y.; Miyasaka, T. Organometal Halide Perovskites as Visible-Light Sensitizers for Photovoltaic Cells. *J. Am. Chem. Soc.* **2009**, *131* (17), 6050−6051.

(2) Lee, M. M.; Teuscher, J.; Miyasaka, T.; Murakami, T. N.; Snaith, H. J. Efficient Hybrid Solar Cells Based on Meso-Superstructured Organometal Halide Perovskites. *Science* **2012**, *338* (6107), 643−647.

(3) Burschka, J.; Pellet, N.; Moon, S. J.; Humphry Baker, R.; Gao, P.; Nazeeruddin, M. K.; Grätzel, M. Sequential Deposition as a Route to High-Performance Perovskite-Sensitized Solar Cells. *Nature* **2013**, *499* (7458), 316−319.

(4) Saliba, M.; Matsui, T.; Domanski, K.; Seo, J. Y.; Ummadisingu, A.; Zakeeruddin, S. M.; Correa-Baena, J. P.; Tress, W. R.; Abate, A.; Hagfeldt, A.; et al. Incorporation of Rubidium Cations into Perovskite Solar Cells Improves Photovoltaic Performance. *Science* **2016**, *354* (6309), 206−209.

(5) Luo, Q.; Ma, H.; Zhang, Y.; Yin, X.; Yao, Z.; Wang, N.; Li, J.; Fan, S.; Jiang, K.; Lin, H. Cross-Stacked Superaligned Carbon Nanotube Electrodes for Efficient Hole Conductor-Free Perovskite Solar Cells. *J. Mater. Chem. A* **2016**, *4* (15), 5569−5577.

(6) Liu, J.; Wang, G.; Song, Z.; He, X.; Luo, K.; Ye, Q.; Liao, C.; Mei, J. FAPb1-xSnxI3 Mixed Metal Halide Perovskites with Improved Light Harvesting and Stability for Efficient Planar Heterojunction Solar Cells. *J. Mater. Chem. A* **2017**, *5* (19), 9097−9106.

(7) Kulbak, M.; Gupta, S.; Kedem, N.; Levine, I.; Bendikov, T.; Hodes, G.; Cahen, D. Cesium Enhances Long-Term Stability of Lead Bromide Perovskite-Based Solar Cells. *J. Phys. Chem. Lett.* **2016**, *7* (1), 167−172.

(8) Liu, C.; Li, W.; Zhang, C.; Ma, Y.; Fan, J.; Mai, Y. All-Inorganic CsPbI2Br Perovskite Solar Cells with High Efficiency Exceeding 13%. *J. Am. Chem. Soc.* **2018**, *140* (11), 3825−3828.

(9) Liang, J.; Wang, C.; Wang, Y.; Xu, Z.; Lu, Z.; Ma, Y.; Zhu, H.; Hu, Y.; Xiao, C.; Yi, X.; et al. All-Inorganic Perovskite Solar Cells. *J. Am. Chem. Soc.* **2016**, *138* (49), 15829−15832.

(10) Chang, X.; Li, W.; Zhu, L.; Liu, H.; Geng, H.; Xiang, S.; Liu, J.; Chen, H. Carbon-Based CsPbBr 3 Perovskite Solar Cells: All-Ambient Processes and High Thermal Stability. *ACS Appl. Mater. Interfaces* **2016**, *8* (49), 33649−33655.

(11) Duan, J.; Zhao, Y.; He, B.; Tang, Q. High-Purity Inorganic Perovskite Films for Solar Cells with 9.72% Efficiency. *Angew. Chem., Int. Ed.* **2018**, *57* (14), 3787−3791.

(12) Jiang, Y.; Yuan, J.; Ni, Y.; Yang, J.; Wang, Y.; Jiu, T.; Yuan, M.; Chen, J. Reduced-Dimensional $α$-CsPbX3 Perovskites for Efficient and Stable Photovoltaics. *Joule* **2018**, *2* (7), 1356−1368.

(13) Aristidou, N.; Eames, C.; Islam, M. S.; Haque, S. A. Insights into the Increased Degradation Rate of CH3NH3PbI3 Solar Cells in Combined Water and O2 Environments. *J. Mater. Chem. A* **2017**, *5* (48), 25469−25475.

(14) Liu, G.; Yang, B.; Liu, B.; Zhang, C.; Xiao, S.; Yuan, Y.; Xie, H.; Niu, D.; Yang, J.; Gao, Y.; et al. Irreversible Light-Soaking Effect of Perovskite Solar Cells Caused by Light-Induced Oxygen Vacancies in Titanium Oxide. *Appl. Phys. Lett.* **2017**, *111* (15), 153501.

(15) Ginting, R. T.; Jeon, M. K.; Lee, K. J.; Jin, W. Y.; Kim, T. W.; Kang, J. W. Degradation Mechanism of Planar-Perovskite Solar Cells: Correlating Evolution of Iodine Distribution and Photocurrent Hysteresis. *J. Mater. Chem. A* **2017**, *5* (9), 4527−4534.

(16) Luchkin, S. Y.; Akbulatov, A. F.; Frolova, L. A.; Tsarev, S. A.; Troshin, P. A.; Stevenson, K. J. Spatially-Resolved Nanoscale Measurements of Grain Boundary Enhanced Photocurrent in Inorganic CsPbBr3 Perovskite Films. *Sol. Energy Mater. Sol. Cells* **2017**, *171*, 205−212.

(17) Wu, N.; Shi, C.; Li, N.; Wang, Y.; Li, M. Preparation of ZnO Nanorod Arrays by Hydrothermal Procedure and Its Application in Perovskite Solar Cells. *Mater. Res. Innovations* **2016**, *20* (5), 338−342.

(18) Commandeur, D.; Morrissey, H.; Chen, Q. Solar Cells with High Short Circuit Currents Based on CsPbBr3Perovskite-Modified ZnO Nanorod Composites. *ACS Appl. Nano Mater.* **2020**, *3* (6), 5676−5686.

(19) Ng, C. H.; Ripolles, T. S.; Hamada, K.; Teo, S. H.; Lim, H. N.; Bisquert, J.; Hayase, S. Tunable Open Circuit Voltage by Engineering Inorganic Cesium Lead Bromide/Iodide Perovskite Solar Cells. *Sci. Rep.* **2018**, *8* (1), 2482.

(20) Huang, A.; Lei, L.; Zhu, J.; Yu, Y.; Liu, Y.; Yang, S.; Bao, S.; Cao, X.; Jin, P. Achieving High Current Density of Perovskite Solar Cells by Modulating the Dominated Facets of Room-Temperature DC Magnetron Sputtered TiO2 Electron Extraction Layer. *ACS Appl. Mater. Interfaces* **2017**, *9* (3), 2016−2022.

(21) Yang, G.; Lei, H.; Tao, H.; Zheng, X.; Ma, J.; Liu, Q.; Ke, W.; Chen, Z.; Xiong, L.; Qin, P.; et al. Reducing Hysteresis and Enhancing Performance of Perovskite Solar Cells Using Low-Temperature Processed Y-Doped SnO2 Nanosheets as Electron Selective Layers. *Small* **2017**, *13* (2), 1601769.

(22) Zhang, X.; Jin, Z.; Zhang, J.; Bai, D.; Bian, H.; Wang, K.; Sun, J.; Wang, Q.; Liu, S. F. All-Ambient Processed Binary CsPbBr3−CsPb2Br5 Perovskites with Synergistic Enhancement for High-Efficiency Cs−Pb−Br-Based Solar Cells. *ACS Appl. Mater. Interfaces* **2018**, *10* (8), 7145−7154.

(23) Teng, P.; Han, X.; Li, J.; Xu, Y.; Kang, L.; Wang, Y.; Yang, Y.; Yu, T. Elegant Face-Down Liquid-Space-Restricted Deposition of CsPbBr3 Films for Efficient Carbon-Based All-Inorganic Planar Perovskite Solar Cells. *ACS Appl. Mater. Interfaces* **2018**, *10* (11), 9541−9546.

(24) Holzwarth, U.; Gibson, N. The Scherrer Equation versus the "Debye-Scherrer Equation". *Nat. Nanotechnol.* **2011**, *6* (9), 534−534.

(25) Pan, D.; Fu, Y.; Chen, J.; Czech, K. J.; Wright, J. C.; Jin, S. Visualization and Studies of Ion-Diffusion Kinetics in Cesium Lead Bromide Perovskite Nanowires. *Nano Lett.* **2018**, *18* (3), 1807−1813.

(26) de Quilettes, D. W.; Zhang, W.; Burlakov, V. M.; Graham, D. J.; Leijtens, T.; Osherov, A.; Bulović, V.; Snaith, H. J.; Ginger, D. S.; Stranks, S. D. Photo-Induced Halide Redistribution in Organic−Inorganic Perovskite Films. *Nat. Commun.* **2016**, *7* (1), 11683.

(27) Lee, S. W.; Kim, S.; Bae, S.; Cho, K.; Chung, T.; Mundt, L. E.; Lee, S.; Park, S.; Park, H.; Schubert, M. C.; et al. UV Degradation and Recovery of Perovskite Solar Cells. *Sci. Rep.* **2016**, *6* (1), 38150.

(28) Shen, D.; Zhang, W.; Xie, F.; Li, Y.; Abate, A.; Wei, M. Graphene Quantum Dots Decorated TiO_2 Mesoporous Film as an Eff
So
(
Zh
Cs
AC
(
Zh
wi
lur
En
(
Lo
by
14
(
Be
Be
in
24

https://doi.org/10.1021/acs.jpcc.1c05714
J. Phys. Chem. C XXXX, XXX, XXX−XXX